Numerical Simulations for Planetary Rovers Safe Navigation and LIDAR Based Localization

Anna Maria Gargiulo
Department of Mechanical and Aerospace Engineering
Sapienza University of Rome
Rome, Italy
gargiulo.1700237@studenti.uniroma1.it

Ivan di Stefano
Department of Mechanical and Aerospace Engineering
Sapienza University of Rome
Rome, Italy
ivan.distefano@uniroma1.it

Antonio Genova
Department of Mechanical and Aerospace Engineering
Sapienza University of Rome
Rome, Italy
antonio.genova@uniroma1.it

***Abstract*—Space exploration rovers are designed to investigate the surface of celestial bodies in the Solar System, seeking habitability conditions and biosignatures. These vehicles are equipped with instrumentation and sensors that allow accomplishing *in-situ* operations. To increase their access capability to harsh environments, onboard systems are included to enable obstacle avoidance and slip prediction that represent fundamental functionalities for safe navigation. This work focuses on the implementation of a method that accurately reproduces the wheel-soil interaction and predicts rovers' performances in different scenarios (*e.g.*, cloddy/drift terrain type, steep terrains). We implemented a 3D model of a rover to simulate its navigation with obstacles on the path. Our estimated trajectory is obtained through the Light Detection And Ranging (LIDAR) data processing, which enables the simultaneous localization and mapping (SLAM).**

Keywords—Navigation, path planning, obstacle avoidance, simultaneous localization and mapping, LIDAR

I. Introduction

Rover navigation on planetary surfaces is strongly affected by the explored environment. The effect of low–gravity has a significant impact on the wheel-soil interaction, causing a reduction in traction [1]. High slippery terrains, slopes and obstacles could endanger the mission, limiting the rover locomotion [2]. The NASA's rover Spirit, for example, got stuck in soft soil, descoping the mission to a stationary science platform [3]. To cope with these hazards, rovers host onboard subsystems devoted to obstacle avoidance and slip prediction [4]. Soil Properties and Object Classification (SPOC) is a software built upon a deep Convolutional Neural Network (CNN) that labels various terrain types analyzing Curiosity's NavCam images and improves the mission path planning [5]. These capabilities expand rovers' autonomy to enhance the number of sites they can visit and the experiments they can conduct. Predictions on the rover performances are usually based on empirical approaches (*i.e.*, the model is built by learning a nonlinear approximation function that maps terrain slopes to the measured slip through a standard nonlinear regression technique [5]). A drawback of this method is that data must be collected through many experiments on Earth (data from past rover missions are not useful, mainly due to differences in size and mass of the rovers) [5,6]. An alternative approach is based on identifying soil parameters [7]. A better modeling of the terrain allows us to accurately define the dynamical equations [8]. By assuming a rigid wheel on soft soil to represent the wheel–soil interaction [9], previous studies (*e.g.*, [10]) carried out simulations of the traverses of the NASA's Mars Exploration Rovers (MER) Spirit and Opportunity. An independent approach was proposed by Gibbesch & Schäfer [11] through the integration of the Multibody System simulation to investigate the dynamic of vehicle, including the suspension. This work is also based on the rigid wheel assumption, which is not adequate to simulate the trajectory of rovers equipped with flexible wheels, *e.g.*, ESA's ExoMars rover [12].

Our numerical simulations were carried out with an accurate modeling of the compliance of both wheel and ground [13-14]. A 3D model of the rover was developed by using size and mass of the ESA's rover ExoMars [15] (Fig. 1). Different terrain types and slopes were also accounted for to investigate the discrepancies in the evolution of the rover trajectory.

To enable an accurate estimation of the rover position across different environments that include hazards, we implemented a simultaneous localization and mapping (SLAM) system with a Light Detection And Ranging (LIDAR) instrument. The SLAM algorithm provides precise localization of the rover and identification of the hazards along the path [16]. The LIDAR range data are well-suited to measure the relative distance between the vehicle and the obstacles [17, 18], yielding higher accuracies compared to Wheel Odometry (WO).

II. Space Rover Navigation Modeling

A. Dynamical Model

We modeled the rover's dynamical equations by assuming compliant wheels on compliant ground. The resistance to the motion acting on the wheels is due to energy

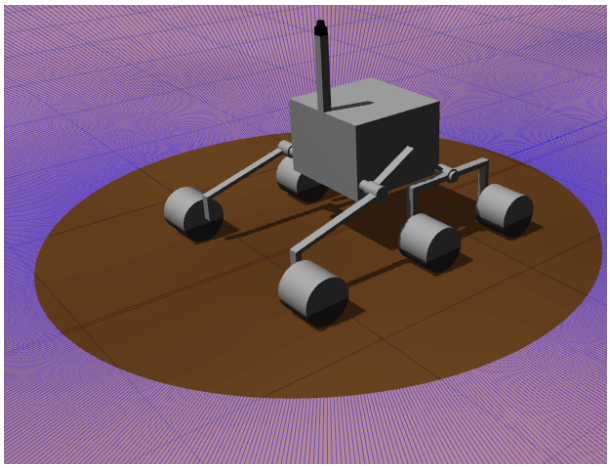

Fig. 1. 3D model of the rover with operative LIDAR sensor in the Gazebo Simulator.

TABLE I. ROVER PARAMETERS: L IS THE WHEEL BASE AND t IS THE DISTANCE BETWEEN THE KINGPIN AXES OF THE WHEELS. v_{max} AND v_c REPRESENT THE ROVER'S MAXIMUM AND NOMINAL SPEED, RESPECTIVELY.

Parameter	m [kg]	p_{gr} [kPa]	R_w [m]	b [m]	L [m]	t [m]	v_{max} [m/h]	v_c [m/h]
Value	310	14.6	0.1425	0.12	1.35	1.2	100	40

dissipation in both wheel and ground. This hypothesis is suitable to represent motion on unprepared ground, as planetary surfaces. The wheel-soil interaction results in a vertical force F_z, a longitudinal force F_x, a lateral force F_y, and an aligning moment M_z acting on each vehicle's wheel [13, 14, 19]. We modeled these forces as follows:

$$F_z = R_w b \int_{\theta_l}^{\theta_0} [\sigma_z(\theta)\cos(\theta) + \tau_x(\theta)\sin(\theta)]\mathrm{d}\theta + 2bx_a p_{gr} = \frac{mg}{n_w}\cos(i) \quad (1)$$

$$F_x = R_w b \int_{\theta_l}^{\theta_0} [-\sigma_z(\theta)\sin(\theta) + \tau_x(\theta)\cos(\theta)]\mathrm{d}\theta + R_w b \int_{-\theta_l}^{\theta_l} \tau_x(\theta)\mathrm{d}\theta \quad (2)$$

$$F_y = -R_w b \int_{-\theta_l}^{\theta_0} \tau_y(\theta)\mathrm{d}\theta - R_w b \int_{-\theta_l}^{\theta_0} F_{yb}[R_w - h(\theta)\cos(\theta)]\mathrm{d}\theta \quad (3)$$

$$M_z = -R_w^2 b \int_{-\theta_l}^{\theta_0} \tau_y(\theta)\sin(\theta)\,\mathrm{d}\theta \quad (4)$$

where R_w and b are the radius and the width of the rover's wheel, respectively; n_w is the number of the vehicle's wheels; σ_z is the normal load, and τ_x and τ_y are the longitudinal and lateral shear stresses, respectively; x_a is the x-coordinate where the pressure exerted on the ground exceeds the pressure p_{gr} needed to deform the tire (that stands for an equivalent stiffness of flexible wheels); m is the vehicle's mass, g is the gravitational acceleration of the planet and i is the slope angle. F_{yb} is the bulldozing force per unit width and h is the sinkage of the wheel; θ_0 and θ_1 are the angles that identify the portion of the wheel involved in the contact with the ground and must be computed at each step, solving Eq. (1).

The longitudinal slip σ is a key measurement that constrains the traverse in highly-unstructured and natural terrains. This parameter measures the difference between the commanded speed of the vehicle ΩR_w (controlled through the wheels angular speed) and its actual speed V:

$$\sigma = \begin{cases} \frac{\Omega R_w - V}{\Omega R_w} & \textit{in driving} \\ \frac{\Omega R_w - V}{V} & \textit{in braking} \end{cases} \quad (5)$$

Once all the interaction forces have been introduced, the method integrates the full set of equations of motion reported in the Model for High Speed Cornering [19, 20]. The vehicle's trajectory and the evolution of the velocity components, angular speed and acceleration are obtained straightforwardly.

TABLE II. TERRAIN PARAMETERS

Soil Properties	**Soil Types**		
	Cloddy	***Mixed Drift-Cloddy***	***Drift***
c [Pa]	170	220	530
Φ [deg]	37.0	33.1	26.4
n [-]	1	1	1
k_c [N/m^{n+1}]	1400	1400	1400
k_Φ [N/m^{n+2}]	820000	820000	820000
K_x, K_y [m]	0.016	0.016	0.016
ρ [kg/m^3]	1550	1350	1150

B. Traversability of Demanding Terrains

We present here the results of numerical simulations that account for extremely steep terrains (*i.e.*, 21° and 26° slopes) with different properties (*i.e.*, cloddy, mixed drift-cloddy and drift). These mission scenarios are consistent with ExoMars extreme operation conditions [15]. Table 1 reports physical and geometrical properties of the modeled rover [15]. Table 2 reports the parameters that define a terrain type, including cohesion c, internal friction angle ϕ, soil cohesive and frictional moduli k_c and k_ϕ, exponent of sinkage n, moduli of the shear deformation in x and y direction K_x and K_y and density ρ [21, 22]. The properties of the soil directly affect the values of normal load σ_z and longitudinal and lateral shear stresses τ_x and τ_y, determining the contact dynamics. The effects of the different terrains types are included in the dynamical model, impacting on the rover's performances. Each simulation case is based on the assumption of homogeneous and constant soil properties.

A Proportional Derivative (PD) control of the commanded speed was implemented to enable uphill and downhill motion, preventing from the locking condition and higher actual speed than v_{max}. The control was designed to maintain the actual speed of the vehicle as close as possible to the nominal speed v_c. We assume a constant steering angle of the wheels (δ=4°) and initial speed V_0=38 m/h.

Fig. 2 (a) and Fig. 2 (c) show the trajectories of the rover with different terrain properties. When the rover traverses a 21° slope with cloddy soil, it turns around reaching the initial orientation. A mixed drift-cloddy soil leads to a different path that diverges from a closed loop. The steering angle adopted in this simulation is not sufficient to deviate the rover's path from a straight line in case of a drift terrain. Different trajectory configurations were also obtained with a steeper terrain with 26° slope for both mixed drift–cloddy and cloddy soil. Fig. 2 (b) shows that the longitudinal slip for a 21° slope reaches the maximum value in the case of drift soil (σ=0.71), which suggests the harsh conditions due to this terrain. Fig. 2 (d) reports the longitudinal slip for the 26° slope traverse, indicating similar slippage for a mixed drift–cloddy soil (σ=0.70) compared to a drift soil with 21°.

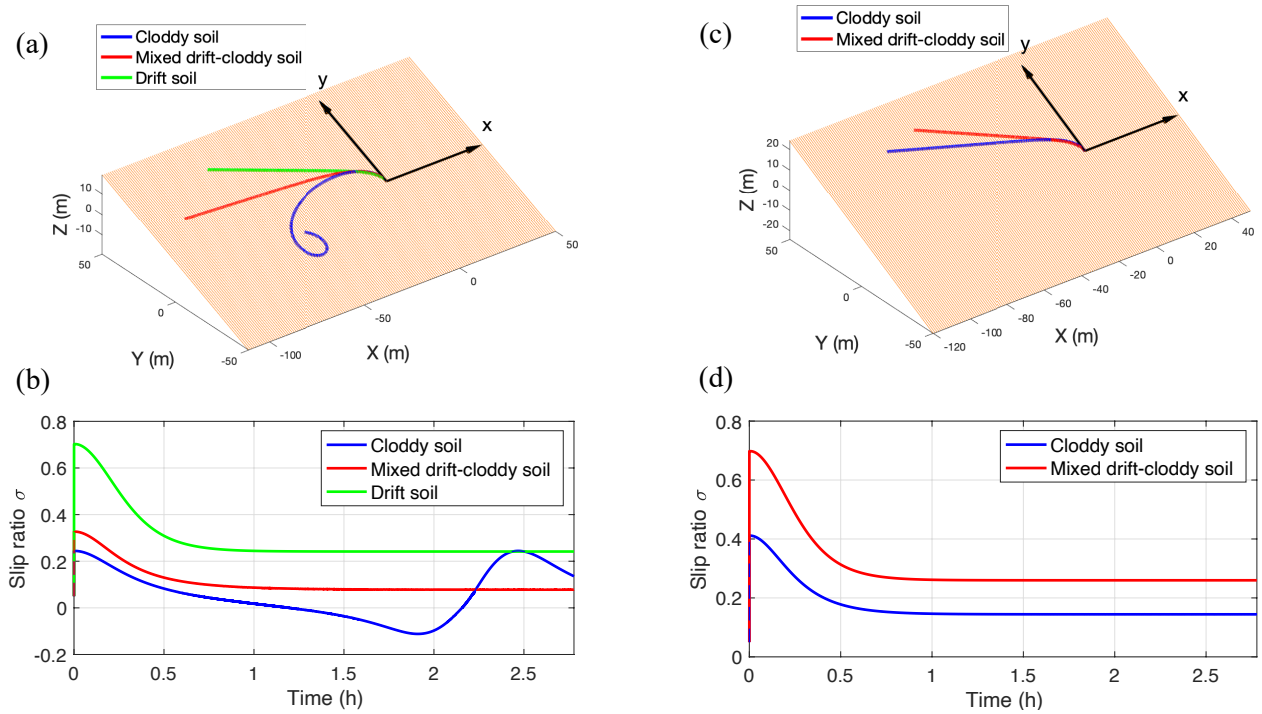

Fig. 2. Rover's trajectories (a-c) and slippage conditions (b-d) over different terrain types for 21° and 26° slope traverse, respectively.

Our results demonstrate the trafficability limits across terrains with different properties [23]. Higher slopes would yield slip ratios close to 1. Therefore, slopes ≤26° and ≤21° are the thresholds for mixed drift-cloddy soil and for drift soil, respectively. These results are in full agreement with previous works (*e.g.*, [15]).

III. Simulated Trajectory and Measurements

An accurate modeling of the surface properties and its interaction with the rover's wheels allow us to simulate the traverse of wheeled vehicles across a Martian-like environment. A thorough definition of the dynamical model is fundamental to determine the evolution of the rover's trajectory from a starting point to a target, and to simulate the measurements of the instruments that are used to reconstruct the path. A precise knowledge of the rover's position across the environment is a key factor for safe navigation.

The mission scenario was conceived by accounting for a coarse soil (cloddy) with several hazards, such as rocks, randomly distributed across the site. The local reference frame (*X, Y*) is supposed to be centered in the initial position of the rover. The *X* axis points eastwards and the *Y* axis northwards. The rover path was planned to reach a specific target located at $(X_f^*, Y_f^*) = (100.0,\ 350.0)$ m in the local reference frame. The rover's initial speed was $v(t_0) = 38$ m/h=$1.056 \cdot 10^{-2}$ m/s. To achieve this objective by avoiding the obstacles, whose coordinates, in this phase, are supposed to be perfectly known, we implemented the following control strategy. We adopted a sequence of steering techniques that allows the rover to follow a fixed direction and to move with constant steering angle. When the distance between the rover and the target is less than 20 m, a proportional control is used for the steering angle and reducing the commanded speed v_c.

Once the path was obtained, the resulting trajectory was simulated by computing and integrating Eqs. (1-4) to account for the interaction forces acting on each wheel [19]. The state of the rover was updated at each time step. During the traverse, we simulated the LIDAR range measurements that were used as input in our trajectory estimator.

Fig. 3 shows the simulated trajectory. The rover is able to reach the final position $(X_f, Y_f) = (100.152, 349.831)$ m with a limited approaching velocity, $v(t_f) = 1.340 \cdot 10^{-4}$ m/s. The selected path represents a safe option, whereas the shortest trajectory reported in magenta is discarded because of the presence of hazards.

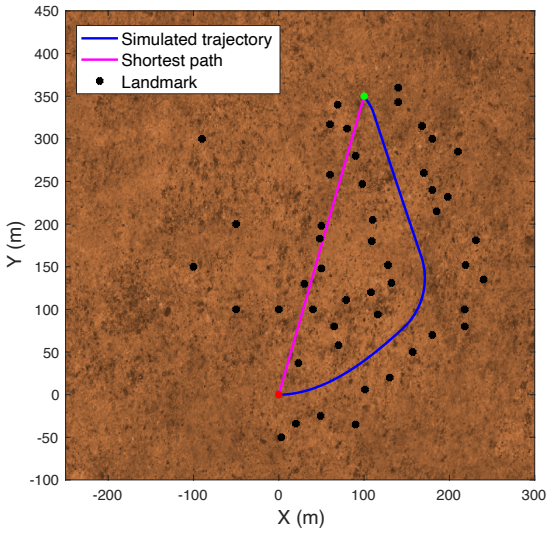

Fig. 3. Simulated trajectory (blue) and straight-line path (magenta) across the landmarks (black dots) between starting (red dot) and target (green dot) position.

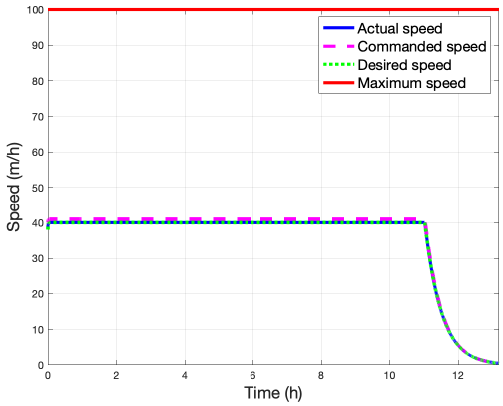

Fig. 4. Evolution of the rover's speed vs time.

The actual speed of the rover accurately follows the desired trend (Fig.4), and a small delay affects the interval when the rover slows down.

IV. LIDAR Based Localization System

The localization system was designed with the goal to reconstruct the rover trajectory and to determine the hazards location. The sensors of this system consist of WO to measure the angular rate of the wheels and, consequently, the distance d travelled, Inertial Measurement Unit (IMU) with accelerometers and gyroscopes to provide the rover's orientation (yaw angle, ψ), and an omnidirectional LIDAR to determine the relative distance between the rover and a landmark.

First, the state of the rover $q = (x, y, \psi)$ and the covariance matrix P are propagated according to:

$$\bar{q}_{k+1} = f(\hat{q}_k, \delta_k, \nu_k) \tag{6}$$

$$\bar{P}_{k+1} = F_q \hat{P}_k F_q^T + F_\nu V F_\nu^T \tag{7}$$

where $\delta_k = (\delta_d, \delta_\psi)$ are the distance and yaw measurements provided by WO and IMU, respectively; and ν is the associated error. WO and IMU errors are modeled as a zero mean multivariate Gaussian noise (σ_d=3 cm and σ_ψ=0.8°). The initial covariance matrix $\bar{P}_0$ is a diagonal matrix with σ_x=σ_y =5 m and σ_{yaw}= 0.001°, V is the variance matrix and F_q and F_v are the matrices of the partial derivatives of Eq. (6) with respect to q and ν, evaluated considering zero noise [24]. By applying WO and IMU only, the estimated trajectory would diverge from the reference path (Fig. 5) because of systematic errors that accumulate over time. A further source of error is that WO does not include any information on the wheel slippage. The instability in the reconstructed trajectory is shown with the uncertainty ellipses of the rover's state (Fig. 5), whose size increases over time, leading to a poor knowledge of the rover's position in proximity of the target.

A more accurate estimation of the rover's trajectory is then based on the processing of the LIDAR range measurements. These data are acquired onboard the rover with a 60-s sampling rate. The availability of these observables relies on the presence of landmarks within the instrument field of view (FOV) and their relative distance from the rover that should be lower than the LIDAR

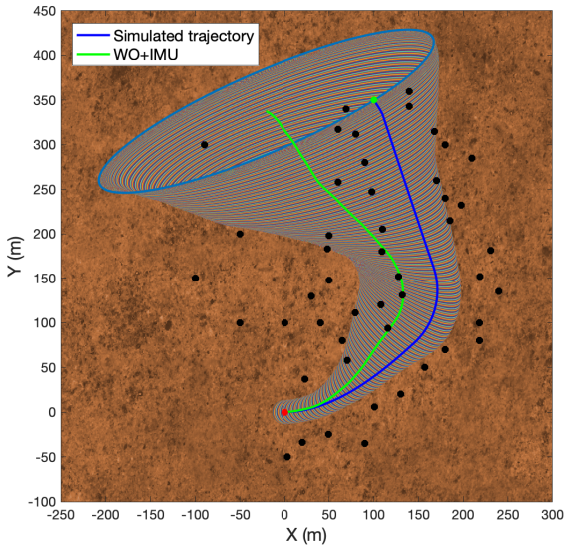

Fig. 5. Reconstructed trajectory (blue) and uncertainty ellipses based on WO and IMU measurements only vs simulated trajectory (green).

maximum range (80 m). A new observable is processed to improve the estimation of the rover's position and to identify the landmark location. The first time a landmark j is detected, its coordinates are included in the state vector $\bar{q}' = (x, y, \psi, x_1, y_1, \dots, x_j, y_j)$ [25]. These additional variables are computed according to:

$$g(q, z_j) = (x_j, y_j)^T = \begin{pmatrix} x + r_j \cos(\psi + \beta_j) \\ y + r_j \sin(\psi + \beta_j) \end{pmatrix} \tag{8}$$

where $z_j = (r_j, \beta_j)$ is the observed observable, *i.e.*, the LIDAR range and bearing angle measurements associated with the j-th landmark; z is affected by the noise w associated with the lidar sensor. The noise has a zero mean Gaussian distribution with σ_r =2 cm and σ_β =0.3°. The covariance matrix is now defined as follows:

$$\bar{P}'_{k+1} = Y \begin{pmatrix} \bar{P}_{k+1} & 0 \\ 0 & W \end{pmatrix} Y^T \tag{9}$$

W is the covariance matrix of the LIDAR sensor noise and Y is the insertion Jacobian:

$$Y = \frac{\partial q'}{\partial z} = \begin{pmatrix} I_{n \times n} & 0_{n \times 2} \\ \bar{G}_x & G_z \end{pmatrix} \tag{10}$$

$\bar{G}_x = (\frac{\partial g}{\partial q}, 0_{2 \times n-3})$ and $G_z = \frac{\partial g}{\partial z}$. The matrix size n is the length of the state vector q prior to the identification of the new landmark.

If the same landmark is observed afterwards, the state and the covariance matrix are updated through an Extended Kalman Filter (EKF) algorithm:

$$\hat{q}_{k+1} = \bar{q}'_{k+1} + K_{k+1}[z_{k+1} - h(\bar{q}'_{k+1})] \tag{11}$$

$$\hat{P}_{k+1} = [I - K_{k+1} H_{k+1}] \bar{P}'_{k+1} \tag{12}$$

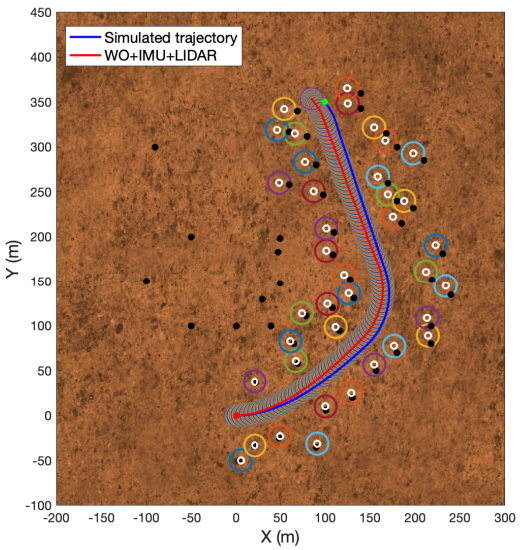

Fig. 6. Reconstructed trajectory (red) and uncertainty ellipses obtained through the processing of WO, IMU and LIDAR measurements vs simulated trajectory. The estimated location (white dots) and uncertainty ellipses of the landmarks are reported in comparison with their simulated distribution (black dots).

h is the computed observable and K is the Kalman gain, computed at each step:

$$K_{k+1} = \overline{P}'_{k+1} H_{k+1}^T S^{-1} \quad (13)$$

where $S = H_{k+1}\overline{P}'_{k+1}H_{k+1}^T + H_w W H_w^T$; H is the matrix of the partial derivatives of the observed observables with respect to q; $H_w$is the derivative of the observed observables with respect to w. The non-zero terms of H are associated with the vehicle's state and the j–th landmark coordinates. If the LIDAR detects a group of landmarks the system randomly selects one of them to update the state vector and the covariance matrix.

The additional information provided by the LIDAR significantly improves the performances of the localization system. Fig. 6 highlights that the reconstructed trajectory slightly diverges from the simulated path because of WO errors. The accumulated integration errors also affect significantly the estimate of the landmarks locations, leading to larger discrepancies as the distance from the starting position increases. Fig. 7 (a) shows that the errors in the rover's position estimates obtained through the SLAM method are almost one order of magnitude lower than those associated with WO only at the end of the path. Furthermore, the SLAM method allows reducing the uncertainty on the estimated position (Fig. 7 (b)).

The SLAM technique mitigates the drift errors of position and heading angle that accumulate over time in WO. A drawback of this method is that the SLAM performances are deeply affected by featureless environments that compromise the accuracy of localization and map updating [26].

V. Summary

Accurate models of the rover's dynamics were implemented to carry out realistic simulations of rover's operations in different environments. Since soil properties

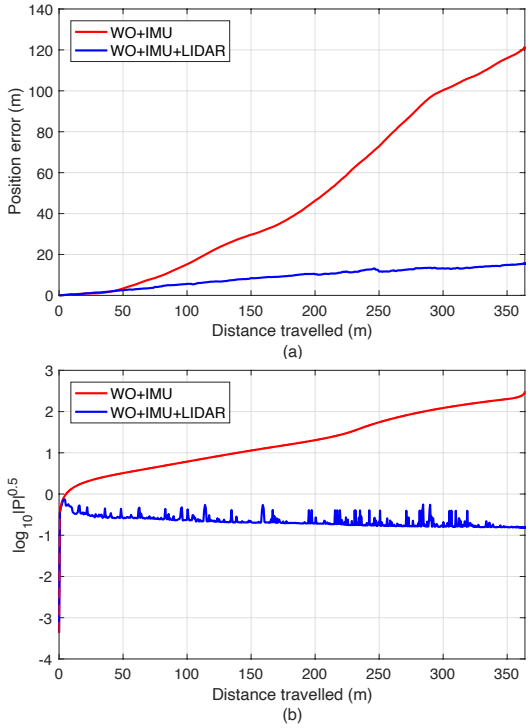

Fig. 7. (a) comparison of the position error obtained through WO and IMU trajectory reconstruction and through SLAM method. (b) Square root of the determinant of vehicle's state covariance matrix vs the distance travelled.

deeply affect rover navigation, our results account for wheel-soil interaction forces.

By analyzing different terrain conditions and types, we reproduced mission scenarios that are in agreement with the ExoMars expected performances [15]. An accurate modeling of the dynamical equations allowed us to simulate the navigation of a rover across a site with obstacles. By implementing WO and LIDAR instruments, we processed the simulated data to investigate the benefits of simultaneous localization and mapping. Our results are consistent with the expectation, supporting that the adopted technique is well-suited for safe navigation of rovers across rough terrains.

Acknowledgments

The software developed to carry out the presented simulations is based on Gazebo simulator libraries [27] (http://gazebosim.org).

References

[1] P. Niksirat, A. Daca and K. Skonieczny. "The effects of reduced-gravity on planetary rover mobility". The International Journal of Robotics Research; vol. 39 (7): pp. 797-811, 2020.

[2] R. A. Lindemann and C. J. Voorhees. "Mars Exploration Rover mobility assembly design, test and performance". In: IEEE International Conference on Systems, Man and Cybernetics, Waikoloa, HI, USA; 12 Oct 2005.

[3] J. L. Callas. "Mars Exploration Rover Spirit end of mission report", Pasadena, CA; Tech. Rep. JPL D-92756, JPL publication, 16–2, 2015.

[4] S. B. Goldberg, M. W. Maimone, and L. Matthies. "Stereo vision and rover navigation software for planetary exploration". *IEEE* Aerospace Conference, vol. 5. Big Sky, Montana, March 2002.

[5] B. Rothrock, J. Papon, R. Kennedy et al. "SPOC: Deep Learning-basd terrain classification for Mars Rover Missions". In: AIAA SPACE 2016, Long Beach, CA; Sep 13–16, 2016.

[6] E. Bakker, H. B. Pacejka and L. Lidner. “A new tire model with an application in vehicle dynamics dtudies”. SAE Technical Paper 890087, 1989.

[7] H. A. Perko, J. D. Nelson and J. R. Green. “Mars soil mechanical properties and suitability of Mars soil simulants”. Journal of Aerospace Engineering, vol. 19 (3): pp. 169–176; 2006

[8] G. Ishigami, A. Miwa, K. Nagatani and K. Yoshida. “Terramechanics-based model for steering maneuver of planetary exploration rovers on loose soil”. J. Field Robotics, 24 (3), pp. 233-250; 2007.

[9] J. Y. Wong. “Predicting the performances of rigid rover wheels on extraterrestrial surfaces based on test results obtained on earth”. Journal of Terramechanics, vol. 49 (1): pp. 49–61; 2012

[10] F. Zhou, R. E. Arvidson, K. Bennett et al. “Simulations of Mars rover traverses”. Journal of Field Robotics, vol. 31 (1): pp. 141–160, 2014.

[11] A. Gibbesch and B. Sch ä fer. “Multibody system modelling and simulation of planetary rover mobility on soft terrain”. In: The 8th International Symposium on Artificial Intelligence, Robotics and Automation in Space–iSAIRAS, Munich, DE. Sep 5–8, 2005.

[12] D. Grandy, N. Panek, G. Routhier and P. Ridolfi. “Development and qualification of the ExoMars Bogie Electro–Mechanical Assembly (BEMA) rotary actuators”. In: 18th European Space Mechanisms and Tribology Symposium, Munich, DE, Sep 18–20, 2019.

[13] M. G. Bekker. “Introduction to Terrain-Vehicle Systems”, The University of Michigan Press, Ann Arbor, USA, 1969.

[14] J. Y. Wong. “Terramechanics and off-road vehicle engineering: terrain behaviour, off-road vehicle performance and design”. Amsterdam, NL: Elsevier, Second edn, 2010.

[15] ESA ExoMars landing site working group. “ExoMars 2018 landing site selection user’s manual”. ESA Ref.: EXM-SCI-LSS-ESA/IKI-003. 2013.

[16] H. Durrant–Whyte and T. Bailey. “Simultaneous localization and mapping: part I”. IEEE Robotics & Automation Magazine, vol. 13 (2): pp. 99–110; 2006.

[17] I. M. Rekleitis, J.-L. Bedwani and E. Dupuis. “Autonomous planetary exploration using LIDAR data”. In: IEEE International Conference on Robotics and Automation (ICRA), Kobe, JP, May 12–17, 2009.

[18] A. Shaukat, P.C. Blacker, C. Spiteri and Y. Gao. “Towards camera-LIDAR fusion-based terrain modelling for planetary surfaces: review and analysis”. Sensors, vol. 16 (11), 1952; 2016

[19] G. Genta. “Introduction to the mechanics of space robots”. Dordrecht, NL: Springer, 2012.

[20] G. Genta and L. Morello. “The automotive chassis. Volume 2: system design”, Dordrecht, NL: Springer, 2009.

[21] N. Patel, R. Slade and J. Clemmet. “The ExoMars rover locomotion subsystem”, J. Terramechanics, vol. 47, pp. 227–242, 2010.

[22] R. Bauer, W. Leung and T. Barfoot, “Development of a dynamic simulation tool for the ExoMars rover”. The 8th International Symposium on Artificial Intelligence, Robotics and Automation in Space (iSAIRAS); Munich, DE; Sep 5-9, 2005.

[23] G. Ishigami, K. Nagatani, and K. Yoshida. “Slope traversal controls for planetary exploration rover on sandy terrain”, J. Field Robot., vol. 26, pp. 264–286, 2009.

[24] P. Corke. “Robotics, Vision and Control: Fundamental Algorithms in MATLAB”, 2nd ed., Dordrecht, NL: Springer, 2017.

[25] T. Bailey and H. Durrant–Whyte. “Simultaneous localization and mapping (SLAM): part II”. IEEE Robotics & Automation Magazine, vol. 13 (3): pp. 108–117; 2006.

[26] J. Tang, Y. Chen, X. Niu et al. “LiDAR scan matching aided inertial navigation system in GNSS–denied environments”. Sensors, vol. 15 (7): pp. 16710–16728; 2015.

[27] N. Koenig and A. Howard. “Design and use paradigms for Gazebo, an open-source multi-robot simulator”. In: IEEE International Conference on Intelligent Robots and Systems (IROS), Sendai, JP; pp. 2149–2154 vol. 3; Sep 28–Oct 2, 2004.